Atmos. Chem. Phys. Discuss., 13, 23895–23941, 2013
www.atmos-chem-phys-discuss.net/13/23895/2013/
doi:10.5194/acpd-13-23895-2013

Atmospheric Chemistry and Physics Discussions

Aerosols optical and physical characteristics and direct radiative forcing during a "Shamal" dust storm, a case study

T. M. Saeed[1], **H. Al-Dashti**[2], **and C. Spyrou**[3]

[1]Science department, College of Basic Education, Public Authority for Applied Education and Training, Kuwait
[2]Department of Meteorology, Directorate General of Kuwait Civil Aviation, Kuwait
[3]School of Physics, University of Athens, Athens, Greece

Received: 28 May 2013 – Accepted: 19 August 2013 – Published: 11 September 2013

Correspondence to: T. M. Saeed (tm.saeed@paaet.edu.kw)

Published by Copernicus Publications on behalf of the European Geosciences Union.

Abstract

Dust aerosols are analyzed for their optical and physical properties during an episode of dust storm that hit Kuwait on 26 March 2003 when "Iraqi Freedom" military operation was in full swing. The intensity of the dust storm was such that it left a thick suspension of dust throughout the following day, 27 March, resulting in a considerable cooling effect at the surface on both days. Ground-based measurements of aerosol optical thickness reached 3.617 and 4.17 on 26–27 March respectively while Ångstrom coefficient, $\alpha_{870/440}$, dropped to −0.0234 and −0.0318. Particulate matter concentration of diameter 10 µm or less, PM_{10}, peaked at 4800 µg m^{-3} during dust storm hours of 26 March. Moderate resolution imaging spectrometer (MODIS) retrieved optical and physical characteristics that exhibited extreme values as well. The synoptic of the dust storm is presented and source regions are identified using total ozone mapping spectrometer (TOMS) aerosol index retrieved images. The vertical profile of the dust layer was simulated using SKIRON atmospheric model. Instantaneous net direct radiative forcing is calculated at top of atmosphere (TOA) and surface level. The thick dust layer of 26 March resulted in cooling the TOA by −60 Wm^{-2} and surface level by −175 Wm^{-2} for a surface albedo of 0.35. Slightly higher values were obtained for 27 March due to the increase in aerosol optical thickness. The large reduction in the radiative flux at the surface level had caused a drop in surface temperature by approximately 6 °C below its average value. Radiative heating/cooling rates in the shortwave and longwave bands were also examined. Shortwave heating rate reached a maximum value of 2° K day^{-1} between 3 and 5 km, dropped to 1.5 ° K day^{-1} at 6 km and diminished at 8 km. Longwave radiation initially heated the lower atmosphere by a maximum value of 0.2 ° K day^{-1} at surface level, declined sharply at increasing altitude and diminished at 4 km. Above 4 km longwave radiation started to cool the atmosphere slightly reaching a maximum rate of −0.1° K day^{-1} at 6 km.

ACPD
13, 23895–23941, 2013

1 Introduction

On Wednesday the 26 March 2003, amidst the military operation "Iraqi Freedom" Kuwait and the surrounding northeastern region of the Arabian Peninsula was exposed to a dust storm. This dust storm that had already passed through Baghdad a day earlier (25 March) caused a slow down in the advancement of US Army and hampered all military operations for the following 24 h (Atkinson, 2004). It was reported that the dust storm was so strong it blew over a 500 gallon fuel-tanker and injured one soldier. Dust and dust storms interfere with human life and function in various ways. They are known to cause health problems especially to the respiratory system leading to various forms of allergies (Wilson and Spengler, 1996; Griffin and Kellogg, 2004; Griffin, 2007; Achudume and Oladipo, 2009; Leski et al., 2011). Dust storms cause soil loss from dry lands and preferentially remove organic matter and the nutrient-rich lightest particles, thereby reducing agricultural productivity. Furthermore the abrasive effect of the dust storm damages young crop plants (Lyles, 1988; Simonson, 1995; Stefanski and Sivakumar, 2009; Ravi et al., 2010). The reduced visibility associated with all forms of dust phenomena impacts the local economy by affecting aircraft aviation and road transportation (De Villiers and Van Heerden, 2007). In certain occasions of severe dust storm it brings the whole locality to a stand still. On the other hand, dust can also have beneficial effects where it deposits. For example, Central and South American rainforests get most of their mineral nutrients from the Sahara dust fallout (Swap et al., 1992; Youlin, 2002). The iron-poor ocean regions get their iron from the deposited dust (Carbo et al., 2005; Herut et al., 2005; Jickells et al., 2005; Mahowald et al., 2005). Data received from TOMS revealed the Arabian Peninsula as one of the major sources of dust emissions around the world after the African sources (Prospero et al., 2002; Washington et al., 2003; Goudi 2009). The Mesopotamian source region identified by Wilkerson (1991) includes Syria, Iraq, western Iran and northeastern Arabian Peninsula. Dust and dust storms initiated in areas lying between Tigris/Euphrates rivers in southern Iraq, which expands an area between 32° N to 32°17′ E, track their path south-

ACPD
13, 23895–23941, 2013

ward over Kuwait and southeastern parts of the Arabian Peninsula. Investigation of the physical and optical characteristics of dust aerosols is crucial to quantifying their radiative impact on the Earth radiation budget. Radiative forcing by dust particles can lead to either heating or cooling of the climate system depending on their single scattering albedo and the underlying surface albedo (Tegen and Lacis, 1996; Haywood and Boucher, 2000; IPPC, 2007). It can also strengthen the low-level frontogenesis leading to a significant intensification of dust storms (Chen et al., 1994). Furthermore radiative forcing by dust particles modulate the low level jet resulting in a diurnal variation of dust emission over arid and semi-arid regions (Alizadeh Choobari et al., 2013). A lot of ground-based and airborne measurement campaigns mainly in the African, Mediterranean and Asian regions have been conducted in recent years to analyze the optical and physical properties of dust aerosols (Sabbah et al., 2001; Ogunjobi et al., 2003; Kaskaoutis et al., 2008; McConnell et al., 2008; Osborne et al., 2008; Saeed and Al dashti, 2010; Haywood et al., 2011), the frequency of dust outbreaks (Goudi and Middleton 1992; Gao et al., 2003; Kutiel and Fruman 2003) and their sources and transport range (Youlin et al., 2002; Washington et al., 2003; Jie Xuana et al., 2004; Tsolmon et al., 2008). Several case studies of dust outbreaks have been conducted in which direct radiative forcing at the surface and at top of the atmosphere (TOA) have been calculated using ground-based and satellite-based data (Xu et al., 2003; Costa et al., 2006; Prasad et al., 2007; Di Sarra et al., 2008; Pandithurai et al., 2008; Di Biagio et al., 2010; Lemaître et al., 2010; Park et al., 2010; Sharma et al., 2012). The results are highly variable depending on their regional and temporal scales. However the study of a sever dust storm in terms of its optical and physical characteristics and calculations of its radiative impact is quite scares in literature. Therefore we present a case study of an intense dust storm that took place at a critical time of a major military operation. The instantaneous optical and physical properties of the dust aerosols that engulfed Kuwait during the 26 March 2003 dust storm and its subsidence over the following day, 27 March, are investigated from both ground-based data and satellite-based data. The synoptic of the dust storm is discussed in conjunction with local meteorological data.

ACPD
13, 23895–23941, 2013

The atmospheric model SKIRON is employed to model the vertical profile of the dust column. Sources of the dust storm are identified using Total Ozone Mapping Spectrometer (TOMS) aerosol index (AI) images. Finally the Santa Barbra DISORT Atmospheric Radiative Transfer (SBDART) model is used to calculate atmospheric fluxes, radiative forcing and heating/cooling rates at TOA and surface levels at both shortwave and longwave bands of the electromagnetic spectrum.

2 Study site

Kuwait (29°22′ N, 48° E) is located at the north western tip of the Arabian (Persian) Gulf, Fig. 1. Kuwait is a small country that extends from 28°55′ N to 30°1′ N and 46°6′ E to 48°4′ E. It lies between Saudi Arabia, Iraq, and the Arabian (Persian) Gulf. It has about 18 000 km^2 of sandy desert and coastal beaches with an estimated population of about two million. The climate of Kuwait and eastern Saudi Arabia is typical of an arid environment. It is characterized by long, hot, and dry summers; it also has short, warm, and sometimes rainy winters, with a mean of 4 inches of rain in Kuwait and 1 inch in coastal Saudi Arabia. The region is subject to violent storms during the spring and summer seasons. Dust storms are prevalent 5 % all throughout the year in Kuwait, but 3.5 % of the day-time from March to August. During the spring season Kuwait is exposed to strong northwesterly "Shamal" (meaning north in Arabic) winds that characterize the weather during the winter-spring seasonal transition. The "Shamal" wind kicks up fine desert sand and silt along the Tigris and Euphrates river basins. The natural funneling of large air masses by high mountains in Turkey and Iran, combined with the high plateaus in Saudi Arabia, help to funnel air across the Mediterranean into the Arabian (Persian) Gulf (Perrone 1979).

ACPD
13, 23895–23941, 2013

3 Synoptic description

The 26 March dust storm is a typical 24 h "Shamal" dust storm that usually takes place at the Spring-Summer transition. The synoptic of this "Shamal" dust storm is examined over the extended period of 23–28 March 2003. A low pressure system moved eastward from western Libya on 23 March, Fig. 2a, into Egypt, Fig. 2b, with an approximate velocity of 16.66 m s^{-1}. It stirred North African dust and sand and carried it aloft. This surface low was a reflection of an upper trough centered over northern Turkey and the Black Sea, Fig. 3a, which then moved into the southeastern direction, Fig. 3b. By 25 March, Figs. 2c and 3c, the low pressure system had stretched from north of the Mediterranean to its central parts. It resulted in a dust storm over Baghdad. The isotherms, superimposed over the contour lines, are also shown in Figs. 2 and 3. It is wave shaped with the ridge of the wave centered over the depression. This steep gradient isotherm moved along the depression over the whole period (23-28 March). A subtropical high pressure was generated behind the depression causing a cold air advection on the west side of the depression on 26 March. Meanwhile a warm air advection was generated from the southwest towards the eastern side of the depression generating a baroclinic zone. This zone, where the contour lines intersect with the isotherms, continued its movement with the depression in its mature stage on 27 and 28 March. The warm advection caused south and southeasterly wind, known locally as "Kaus" to blow over Kuwait on 26 March. However air stream set in west of the new surface low on 26 March created "Shamal" winds reaching surface speed of 11 m s^{-1} on 26 March, Fig. 4. The depression moved swiftly into Iran in the eastward direction by 27–28 March, Fig. 2e, f. For the 500 hpa levels, Fig. 3d shows that the depression had weakened as it moved into the eastward direction. By 27–28 March, Fig. 3e, f the depression had stalled over northern Arabian Peninsula. The wind field relating to 26 March dust storm over Kuwait is shown in Fig. 4. The isotachs are plotted at different geopotential heights. The plot shows an area of convergence taking place over central Saudi Arabia, the Arabian (Persian) Gulf and Iran. The cold "Shamal" wind blowing from

ACPD
13, 23895–23941, 2013

the Mediterranean was intersected with warm air stream blowing from southern Saudi Arabia resulting in a strong upward motion over Kuwait and southern Iraq. The dust storm thus generated on 26 of March lasted for 7 h starting from 07:00 LTC (+3 UTC). The duration and severity of the dust storm over Kuwait was also exhibited in the horizontal distribution of the vertical motion (ω) at different geopotential heights, Fig. 5. The pressure gradient was as steep as −0.25 at surface level and went up to −0.4 at 500–600 hpa. The severity of this dust storm and the high density of fine dust carried by the "Shamal" and the wind from south of Saudi Arabia had caused a thick suspension of fine dust in the atmosphere that lasted for the following 24 hours (27 March). Kuwait Meteorology Department weather radar system, the METEOR 1600C, installed at Kuwait Airport, recorded the progress of the dust storm on 26 March 2003. Figure 6a shows the radar detection of the dust storm at its early stage, ∼07:30 LT. The Z (reflectivity) display shows the dust engulfing Kuwait within the 60 km zone and extending to the north beyond 120 km display range of the radar. By about 09:30 LT, Fig. 6c, the dust had covered most of Kuwait and extended easterly to the Gulf. The radial velocity scan of the dust storm is depicted in Fig. 6b. At the early hours of the dust storm, the dust was blowing towards the centre from the northwestern direction at an average speed of 11–12 m s^{-1}. The radial velocity image of Fig. 6d captured the moving cloud of dust from the northwestern direction to the south and southeastern direction as the dust evolved and intensified around 09:30 LT.

4 Ground-based versus satellite-based data and the spatial distribution of dust aerosols

Aerosol optical thickness (AOT) measurements were acquired in Kuwait City. A five channel Microtops Sunphotometer (Solar Light Co.) was used to measure the daily AOT at five optical channels; 440, 675, 870, 936 and 1020 nm. The water vapor (WV) column was also measured simultaneously in units of length using the channels 870, 936 and 1020 nm. Ångstrom exponent α was derived using the 440 and the 870 nm

ACPD
13, 23895–23941, 2013

channels according to the equation, (Stephens 1994).

$$\alpha_{870/440} = -\ln(\tau_{870} / \tau_{440}) / \ln(870 / 440). \quad (1)$$

The sunphotometer was calibrated by transferring calibration factors from a master sunphotometer. The master sunphotometer was calibrated using the method of Langley plot performed at Mauna Loa observatory in Hawaii. The calibration was performed at the beginning of the measurement period. The absolute accuracy of measurements is expected to be ±0.02 for the optical thickness, with precision 4 times better. AOT measurements at the five optical channels were highly correlated (r = 0.99). Therefore the AOT of the 675 nm channel which is the most comparable to the mean dust particle size is used to represent the AOT. On the other hand particulate matter concentration of diameter 10 µm or less, PM_{10} (µg m^{-3}), were acquired by the Environmental Protection Agency (EPA) station located in Jahra city, 30 km west of Kuwait City. The station uses the BAM-1020 manufactured by Met One Instruments. The BAM-1020 (which stands for Beta Attenuation Mass monitor) is one of several methods used to continuously monitor particulate matter. The air sampler uses a 10 µm filter at the inlet pipe in order to restrict the particle size of the air sample to a maximum of 10 µm. The BAM-1020 works with a resolution of ±2 µg m^{-3}, and an accuracy of ±8 % of indication for 1 h operation mode, ±2 % compared to Federal Reference Method for 24 h operation mode. A complete description of BAM-1020 operation is found at Gobeli et al. (2008). Finally standard meteorological parameters were obtained from Kuwait Meteorology Department which are measured according to standard meteorological procedures approved by World Meteorological Organization. The meteorological data were acquired on an hourly basis from a tower located at the vicinity of Kuwait International Airport, and rises 10 m above ground level. The meteorological parameters used in this work are wind speed, WS (m s^{-1}), wind direction, WD, horizontal visibility, HV (km), expressed as the lowest horizontal visibility attained and weather phenomena (WP) which indicates the type of weather taking place at a certain time. There are a number of weather phenomena defined by the Meteorological Department of Kuwait,

ACPD
13, 23895–23941, 2013

among them are those associated with the dust phenomena. Dust storm (DS) is associated with strong wind exceeding 9 ms^{-1} and poor horizontal visibility of 1 km or less, whereas rising dust (RD) is associated with moderate wind speed ranging between 6 and 9 ms^{-1} and horizontal visibility between 1 and 5 km. Suspended dust (S), on the other hand, arises when there is a thick suspension of dust in the lower troposphere in the absence of strong wind (WS $\leq$ 6 ms^{-1}) whereby horizontal visibility might deteriorate to 1km or less. Table 1 states the optical and physical measurements obtained on 26–27 March at 11:30 LT together with the corresponding meteorological parameters. Since both AOT measurements are acquired at 11:30 LT, the physical and meteorological parameters were found as the average values of PM_{10}, WS and V between 11:00 and 12:00 LT. Aerosol optical thickness, τ_{675}, reached 3.617 on 26 March and 4.17 on 27 March whereas Ångstrom coefficient, $\alpha_{870/440}$, dropped to −0.0234 and −0.0318 respectively. The negative values of $\alpha_{870/440}$ reflects the dominance of coarse-sized dust particles. At the same time PM_{10} reached 1770 $\mu g\,m^{-3}$ on 26 March and was increased to 2641 $\mu g\,m^{-3}$ the following day at the time that AOT was measured. Figure 7 shows the hourly variations of meteorological parameters and PM_{10} concentrations on 26–27 March. The shaded area represents dust storm hours. The strong southeasterly wind blew over Kuwait with a maximum wind speed of 14 $m\,s^{-1}$ at 00:00 LT of 26 March. As the day broke out it changed direction to northwesterly "Shamal" wind and continued to blow at an average speed of 10 $m\,s^{-1}$ thus causing the dust storm. The blowing dust caused severe reduction in visibility reaching a minimum of 200 m during dust storm hours but 400 m at the time AOT was measured. The associated suspended dust continued to hamper visibility all through the following day, 27 March, whereby visibility reached a minimum value of 300 m between 14:00 to 16:00 LT). By then the wind had lost its momentum and was blowing at a moderate speed of approximately 4 $m\,s^{-1}$ from the north and northwestern direction. The PM_{10} measurement of dust concentration peaked at 4800 $\mu g\,m^{-3}$ during dust storm hours on 26 March, and fluctuated with an average value of 1000 $\mu g\,m^{-3}$ throughout the following day before the visibility improved after 16:00 LT of 27 March. Surface temperature was reduced during dust

ACPD
13, 23895–23941, 2013

storm hours as will be shown later. The relative humidity increased when the wind was southeasterly and decreased when the wind was northerly to northwesterly.

Optical and physical parameters were obtained from Moderate Resolution Imaging Spectrometer (MODIS) on board Terra and Aqua satellites. Three parameters were retrieved; aerosol optical depth (AOD) or thickness at 550 nm channel, AOD_{550}, the Ångstrom coefficient $\alpha_{470/660}$, and the areal aerosol mass concentration (MC) in units of $\mu g\,m^{-2}$, Table 2. Both platforms retrieved elevated values of AOD_{550} that exceeded 3. The corresponding Ångstrom coefficient $\alpha_{470/660}$ was lower on 26 March than 27 March reflecting the dominance of large dust particles over Kuwait in accordance with the ground-based measurements. Consequently the retrieved areal mass concentration of 26 March reached $117.8 \pm 33.9 \mu g\,m^{-2}$ but dropped to $24.7 \mu g\,m^{-2}$ on 27 March. Moreover TOMS aerosol index which is another sensor of dust loading in the atmospheric column (Torres et al., 1998) had retrieved elevated values of 3.77 ± 0.93 for 27 March in comparison to 2.95 ± 0.66 for 26 March, Table 2. The slightly higher AI of 27 March is caused by the elevation of fine dust particles to the boundary layer. A full discussion of ground-based AOT versus MODIS retrieved AOT together with their derived optical and physical properties over the whole month of March 2003 is found in our previous paper, Saeed and Al Dashti (2010).

The RGB image captured by Terra-MODIS satellite, Fig. 8 (left) depicts clearly the intensity of the dust storm that engulfed the eastern side of the Arabian Peninsula on 26 March, whereas its aftermath is shown as a thin layer of dust over the Arabian (Persian) Gulf, Fig. 8 (right). Latitude-longitude maps of AOD_{550} retrieved by Terra-MODIS averaged over the two-day event of 26–27 March showed very limited signal over Kuwait and the surrounding area, Fig. 9. This is most likely due to the over bright signal of dust retrieved by MODIS which was discarded by the applied algorithm as it was confused by the bright signal of clouds. However over a very small area of northern Arabian (Persian) Gulf the AOD_{550} retrieval expressed a high value of 3.22 and above. Similarly the highest mass concentration above $100\,\mu g\,m^{-2}$ was exhibited over the Arabian (Persian) Gulf, Fig. 9. TOMS retrieved aerosol index image is used to probe the source regions

ACPD
13, 23895–23941, 2013

of dust activity and its transport route. Figure 10 shows the AI distribution for 26 and 27 March across the Arabian Peninsula. Two regions of high dust activity or "hot spots" are revealed in Fig. 10 (left) with AI around 3. One of them is located in Kuwait and around the southern parts of Iraq and the other one is in the central southeastern parts of the Arabian Peninsula. As the dust storm stalled and fine dust was raised to beyond 3 km on 27 March, Fig. 10 (right), the hot spots became further defined and expanded to encompass most of the middle southeastern parts of the Arabian Peninsula. The elevated levels of fine dust reached beyond the boundary layer and its high intensity caused AI to exceed 4.5. The first "northern" hot spot is located in Kuwait within the vicinity of the lower Mesopotamian source region which extends from 44°57′–46°17′ E and 31°–32° N (Wilkerson 1991). Middleton (1986a) had demonstrated that this source region has the highest number of dust storms per year compared to other source regions in the Middle East. The second "southern" hot spot is the "Rub'al Khali" (or the Empty Quarter) source region which extends across the middle-southeastern parts of the Arabian Peninsula covering an approximate area of 650 000 km^2, Fig. 11. This vast land of prolific sand is considered as one of the five major sources of dust coming after the Bodélé Depression of south-central Sahara and the western Sahara region of Mali and Mauritania (Washington et al., 2003). The Arabian Peninsula is found to have a maximum mean aerosol index above 2.1. Thus the lower Mesopotamian region which extends to the northern boarders of Kuwait and the Rub'al Khali region form the main source regions of dust transfer over Kuwait.

5 Vertical distribution of the dust layer

The vertical profile of the variation of desert dust concentration with height is important in implementing various radiative transfer models and in the evaluation of radiative forcing and heating rates. According to Liao and Seinfeld (1998), under cloud free conditions, the shortwave radiative forcing at surface level and TOA is not sensitive to the altitude of the dust layer but depends primarily on the reflectivity of the underly-

ACPD
13, 23895–23941, 2013

ing surface, aerosols optical thickness and aerosols single scattering albedo. However the altitude of the dust layer influences the longwave radiative forcing. As the dust layer increases in height its overall temperature decreases and therefore reduces longwave radiative forcing at both TOA and surface level. In the absence of in-situ measurements of the vertical distribution of the dust layer SKIRON atmospheric model is used to simulate the desert dust vertical profile. SKIRON (not an acronym) is an atmospheric model developed at the University of Athens by the Atmospheric Modeling and Weather Forecasting Group, (Kallos et al., 1997, 2006) in the framework of the nationally and European Union (EU) funded projects SKIRON, Mediterranean Dust Experiment (MEDUSE), Atmospheric Deposition and Impact on the Open Mediterranean Sea (ADIOS), and recently Climate Change and Impact Research (CIRCE) and Marine Renewable Integrated Application Platform (MARINA). The atmospheric model is based on the ETA/NCEP model, which was originally developed by Mesinger (1984) and Janjic (1984) at the University of Belgrade, but is heavily modified to include state of the art parameterization schemes for meteorological and desert dust processes (Spyrou et al., 2010). The model includes a 16-category soil characteristics dataset (Miller and White, 1998) that provides detailed information on the soil physical properties, such as porosity and available water capacity. A high-resolution (30 s) global land use and cover database is used which includes urban areas that are classified according to the United States Geological Survey (USGS) into 24-category of land use/land cover system (Anderson et al., 1976). SKIRON incorporates a modal representation to describe the distribution of the aerosol mass over source areas. According to this method, the mass distribution is provided by the three-modal lognormal function of D'Almeida (1987), as described in detail by Zender et al. (2003). Dust production is initiated by the entrainment of large sand-sized particles (~60 µm in diameter) through the process of saltation bombardment (Zender et al., 2003). Clay and silt sized particles are produced when the latter ones impact on the soil downwind of their saltation trajectories (Gillette 1977). These particles with radius $r \leq 10$ µm stay in the atmosphere long enough to be transported over large distances (Zender et al., 2003; Spyrou et al., 2010). The

ACPD
13, 23895–23941, 2013

dust particle size distribution follows a lognormal distribution with mass median diameter equal to 2.524 µm and a geometric standard deviation of 2. The transport mode uses eight size bins with effective radius 0.15, 0.25, 0.45, 0.78, 1.3, 2.2, 3.8, 7.1 µm, similar to the size bins selected by Pérez et al. (2006). The dust particles that are mobilized through the process of saltation bombardment are deposited via dry (diffusion, impaction, gravitational settling) and wet (in-cloud and below-cloud removal) mechanisms. More details on the specific characteristics of the atmospheric model and dust module are provided in Spyrou et al. (2010). In order to generate the vertical profile of dust over our period of interest SKIRON was run over the geographical area shown in Fig. 12.This area extends from 67.2°–21.3° E and 7.6°–44.2° N covering the Arabian Peninsula, parts of east Africa and western Asia. The vertical profile of dust concentration was generated by integrating over the designated area from the surface or near surface level up to 20 km above surface level in 38 levels with a horizontal resolution of 0.2° × 0.2°. The ECMWF reanalysis fields were used to set the initial boundary conditions with a spatial resolution of 0.5° × 0.5°. The lateral boundary conditions were updated every 3 h. The resulting vertical distribution is shown in Fig. 13 for the period of 25–29 March 2003. The severity of 26 March dust storm is clearly shown in Fig. 13 with two pockets of high dust concentration exceeding 1000 µg m^{-3} and extending slightly above 2 km from surface level. The medium sized particles are elevated to approximately 3 km above surface level and the finest dust particles are raised up to 6 km from surface level. Similar profile was obtained by Alpert et al. (2004) who investigated the vertical profile of the Saharan dust at its source and as it gets transported to the Eastern Mediterranean island of Lampedusa and Sede Boker in Israel. Sede Boker, being located at the north western side of the Arabian Peninsula, has similar climatological conditions to Kuwait and therefore the spring season witnesses the highest rate of blowing dust. They found that the desert dust was elevated to approximately 4 to 6 km above ground.

ACPD
13, 23895–23941, 2013

6 Direct radiative forcing

Shortwave (SW) (0.28–3.42 µm), longwave (LW) (3.42–500 µm) and net radiative flux from surface level up to the TOA were calculated, in units of Wm^{-2}, using atmospheric radiative transfer model SBDART, (Ricchiazzi et al., 1998). The model is based on a number of well established radiative transfer models such as Discrete Ordinates Radiative Transfer (DISORT), (Stamnes et al., 1988), LOWTRAN (Kneizys et al., 1983) and MODTRAN (Berk et al., 1983), which were developed by various atmospheric research groups. The direct radiative forcing (DRF) at certain level is defined as the difference in net flux, $\text{flux}_{\circ}$, between the dust laden, $\text{flux}_{\circ,a}$, and dust free, $\text{flux}_{\circ,cl}$, atmosphere at the specific level for shortwave (SW) or longwave (LW) bands of the spectra. Therefore DRF at TOA or surface (surf) levels, $\text{DRF}_{\text{TOA/surf}}$, is

$$\text{DRF}_{\text{TOA/surf}} = \left(\text{flux}_{\circ,\text{TOA/surf}}\right)_a - \left(\text{flux}_{\circ,\text{TOA/surf}}\right)_{cl}. \quad (2)$$

Net fluxes at either TOA or surface level, $\text{flux}_{\circ\,\text{AOT/surf}}$, for SW or LW band of the spectra, were computed as the difference between the net downwelling flux, $\text{flux}_{\circ}\downarrow$, and the net upwelling flux, $\text{flux}_{\circ}\uparrow$.

$$\text{flux}_{\circ\,\text{AOT/surf}} = \text{flux}_{\circ}\downarrow - \text{flux}_{\circ}\uparrow \quad (3)$$

The SBDART model calculates radiative flux at certain level based on aerosols physical and optical properties, surface characteristics, atmospheric characteristics and the solar geometry of the geographic location. Among all these variables the most crucial is the surface reflectivity (or albedo) R_s, AOT τ_λ, aerosols single scattering albedo $\omega_\circ$ and the asymmetry parameter g. The surface albedo is defined as the ratio between reflected radiation and incident radiation. Highly reflective surfaces such as snow have their surface albedo close to 1 whereas dark surfaces such as forests and oceans have low surface albedo close to zero. The aerosols single scattering albedo is defined as the ratio between the aerosols scattering coefficient to the aerosols total extinction coefficient. For high scattering aerosols such as mineral dust $\omega_\circ$ would be close to 1, usually around 0.89, and for low scattering aerosols $\omega_\circ$ can be around 0.76. Low $\omega_\circ$ arises

ACPD
13, 23895–23941, 2013

when aerosols absorption increases, a case usually associated with the presence of atmospheric pollutants such as black carbon. The aerosol asymmetry parameter g, which is a parameter representing the aerosols phase function is more complex in its evaluation as it cannot be measured directly like the former variables. The parameter g represents the average cosine of the scattered radiation angle. It is proportional to the aerosol size; larger particles tend to have larger g. The asymmetry parameter can have values between 0 and 1 where zero represents isotropic scattering and 1 represents total forward scattering. However, most common values of g fall between 0.6 and 0.88. Liao and Seinfeld (1998) had investigated the impact of some of these variables on the net radiative forcing (RF) at both surface level and TOA. They found that under clear sky conditions the SW forcing at either level decreases as surface albedo increases by a factor of $(1\text{-}R_s)$ whereas LW radiative forcing is not sensitive to surface albedo and remains always positive at both levels. On the other hand SW RF has a strong dependence on AOT. The cooling, at both TOA and surface levels, increases linearly as AOT increase. In contrast LW RF is less sensitive to AOT variation, it increases only slightly with the increase in AOT. The RF dependence on single scattering albedo is more complex because it depends on the change in planetary albedo which could vary due to the addition of a thin layer of aerosols. There exist a critical single scattering albedo, ω_{cr}, above which cooling takes place and below which heating takes place. The ω_{cr} is given by Chylek and Coakley (1974) and Seinfeld and Pandis (1998) as

$$\omega_{cr} = \frac{2R_s}{2R_s + \beta(1 - R_s)^2}. \quad (4)$$

Where β is the aerosols upscatter fraction. It has been shown that 10 % of overestimation of g can result in about 12 % reduction in RF (Marshal et al., 1995). Here due to the limitation of our in-situ measurements to AOT only, we have taken the approach of assigning realistic values to some of these variables. Table 3 lists the input parameters of SBDART model that were either measured or estimated. The AOT has been measured and discussed and the associated cosine of the solar zenith angle (CSZA) is stated.

ACPD
13, 23895–23941, 2013

The single scattering albedo, ω_o, was assigned a high value of 0.98 based on recent measurements of scattering and absorption coefficients conducted by the first author in Kuwait City under similar atmospheric conditions of high dust loading and elevated AOT. Moreover similar high value of single scattering albedo has also been reported in literature under high dust loading, (Li et al., 2004; Mallet et al., 2006; Prasad et al., 2007; Markowicz et al., 2008). The asymmetry parameter g is assigned a standard value of 0.73 which is most commonly used for mineral dust (Sokolik and Toon 1999; Quijano et al., 2000; Haywood et al., 2001; Andrews et al., 2006). The HV and relative humidity (RH) were obtained from the hourly meteorological data. The surface albedo R_s of desert surface has been reported in literature to be in the range of 0.3–0.35 (Quijano et al., 2000; Andreae et al., 2002; Mallet et al., 2009). The first author had recently measured surface albedo at different locations in the Kuwaiti desert and at different times of the year and found it be 0.35 for most of the locations and time. Since R_s is not precisely known for our two days of interest, radiative fluxes were calculated for both values of R_s; 0.3 and 0.35. The SBDART model was executed for a mid-latitude summer atmospheric profile using six streams for SW and LW DRF calculations. The total or net DRF were calculated as the sum of SW and LW forcing. The vertical distribution of dust aerosols concentration was estimated from Fig. 9. The dust height was set to 2km and then dropped by a factor of 2 between 2–6 km and then by a factor of 500 between 6–100 km. The DRF results for 26–27 March are stated in Table 4. The DRF of the atmosphere, DRF_{atm}, which is the difference between DRF_{TOA} and DRF_{surf} is also stated. The DRF results stated in Table 4 show clearly that mineral dust aerosols had a major cooling effect on the TOA and surface level through the attenuation of incoming solar radiation and a minor heating effect due to LW absorption. The total effect had been cooling of TOA and surface levels but heating the atmosphere in between. On 26 March the SW DRF reached $-95\,Wm^{-2}$ at TOA and $-204\,Wm^{-2}$ at surface level for surface albedo of 0.3 and was reduced by 26 % at TOA and 10 % at surface level for surface albedo of 0.35 making it -70 and $-183\,Wm^{-2}$ respectively. The reduction in DRF at both TOA and surface level as the surface albedo increase is due to the en-

ACPD
13, 23895–23941, 2013

hancement of scattering with the surface (Liao and Sienfeld, 1998). On 27 March the SW DRF increased slightly, in the negative, due to the slight increase in AOT. On the other hand the LW contribution to DRF was almost invariant to the changes in surface albedo and very similar for both days of interest with an average of 11 Wm^{-2} at TOA and 9 Wm^{-2} at surface level. This large amount of negative forcing had caused the surface temperature to drop by approximately 6 °C below its average value on both days of interest, Fig. 14. The negative forcing at both TOA and surface level had caused heating of the atmosphere by 111 Wm^{-2} for $R_s = 0.3$ and 115 Wm^{-2} for $R_s = 0.35$.

Quantification of radiative forcing over the Arabian (Persian) Gulf has been quite scarce for regular dust loading and almost non for extreme dust loading. One study was conducted in the United Arab Emirates by Markowicz et al. (2008) to calculate the average aerosol diurnal surface forcing during the summer months of August and September of 2004. They found the RF at surface level to be −20 Wm^{-2} when AOT was 0.45 and single scattering albedo was 0.93 at 500 nm. Some studies had quantified RF caused by dust storms over the Indian Subcontinent. For example Sharma et al. (2012) calculated RF over Patiala in India for six days of high dust loading ($\tau_{500} = 1 \pm 0.51$) and found the average RF to vary between −50 and −100 Wm^{-2} at surface level and −10 and −25 Wm^{-2} at TOA. In another study Prasad et al. (2007) calculated RF over Kanpur-India and found the average RF at surface level to be −57.5 Wm^{-2} and −13.5 Wm^{-2} at TOA during the months of April and May where τ_{500} reached 1.44, $\omega_{500} = 0.92 \pm 0.03$ and $R_s = 0.2 - 0.23$. Similarly Pandithurai et al. (2008) calculated RF over New Delhi-India during the dusty season of March through June 2006 and found the net RF at surface level to increase from −30 Wm^{-2} for March to −84 Wm^{-2} for June whereas net RF at TOA increased from −3.2 Wm^{-2} for March to 43 Wm^{-2} for June ($\omega_{500} \approx 0.84$–$0.74$ $\tau_{500} \approx 0.55$–1.18). Mallet et al. (2009) investigated the effect of dust aerosols on the surface and TOA radiation budget as well as on surface temperature over West Africa. They found that during an intensive dust episode the SW radiation decreased at the surface by a regional mean of −137 Wm^{-2} which lead to a reduction in surface temperature by 4°C. This is quite in agreement with our results

ACPD
13, 23895–23941, 2013

except that the radiative forcing calculated here is larger due to the instantaneous estimation over a very small region. They also found that TOA SW cooling dominated the net forcing and reached a regional mean of $-12\,\mathrm{Wm}^{-2}$.

7 Radiative heating rate

Atmospheric heating/cooling rate, $\Delta T/\Delta t$, in units of $^{\circ}\mathrm{K\,day}^{-1}$, due to the interaction of SW and LW radiation by mineral dust have been simulated by SBDART following the equation.

$$\frac{\Delta T}{\Delta t} = \frac{-1}{\rho_{\mathrm{air}} \cdot C_p} \cdot \frac{\Delta F_{\mathrm{net}}}{\Delta z} \tag{5}$$

Where ρ_{air} is air density which equals $1.17\,\mathrm{kg\,m}^{-3}$ and C_p is specific heat of dry air which equals $1004.67\,\mathrm{J\,kg}^{-1}\mathrm{K}^{-1}$. The factor $\Delta F_{\mathrm{net}}/\Delta z$ is calculated as the ratio between the net flux ΔF leaving a layer of atmosphere of thickness Δz and the thickness of that layer (Carlson and Benjamin 1980; Quijano et al., 2000; Petty 2006). Net heating/cooling rates were calculated in LW and SW bands as the difference in heating/cooling between the dust laden atmosphere of 26 March and a hypothetically dust free atmosphere. Figure 15 plots the variation in heating/cooling with altitude for surface reflectivity of 0.3 and 0.35. The heating/cooling profile for 27 March is quite similar to that of 26 March and hence omitted. The heating of the atmosphere within the dust layer is associated primarily with SW absorption by mineral dust which reached a maximum of $0.2\,^{\circ}\mathrm{K\,day}^{-1}$ at atmospheric layers of 3 to 5 km, Fig. 15. Although heating rates are affected by the reflectivity of the under lying surface (Bierwirth et al., 2009) it is found here that the difference in heating/cooling rates between the two surfaces to be quite small. On the other hand emission in the LW radiation caused a declining heating profile at the first 4 km with a maximum of $0.2\,^{\circ}\mathrm{K\,day}^{-1}$ at surface level. This slight heating is due to the abundance of coarse-sized dust particles near the surface which

ACPD
13, 23895–23941, 2013

through a relatively small but yet significant amount of absorption tend to heat the atmospheric layers adjacent to the surface. Above 4 km LW radiative switched to cooling due to the dominance of fine dust particles and reached a maximum of $-0.1\,^{\circ}\mathrm{K\,day^{-1}}$ at 6 km. Beyond 7 km both SW and LW heating/cooling rates diminished. This profile of heating/cooling rate mirrors SKIRON simulation of the dust vertical profile (Fig. 13) whereby the coarse-sized dust particles are concentrated in the first 3 km and the fine dust particles are elevated to 6 km. Comparable results were obtained by Mohalfi et al. (1998) who investigated heating rates during dust outbreaks over Saudi Arabia using Florida State University Limited Area Model. They found that dust particles had a significant affect over the SW radiation which caused heating rate to reach almost $2^{\circ}\mathrm{K\,day^{-1}}$ at about 6 km and $3\,^{\circ}\mathrm{K\,day^{-1}}$ at about 8 km. Similarly Mallet et al. (2009) investigated the heating rate over West Africa and found that the maximum SW heating rate occurred within the dust layer with values between $4–7\,^{\circ}\mathrm{K\,day^{-1}}$ and LW heating rate between $-1–0.2\,^{\circ}\mathrm{K\,day^{-1}}$.

8 Summary and conclusion

The Arabian Peninsula is one of the five major sources of mineral dust around the globe. But yet only few studies have been conducted on the characterization of dust properties of the Arabian Peninsula and virtually no study exist, to the best knowledge of the authors, on the radiative impact of a dust storm in the Arabian Peninsula. In this case study we examine the optical, physical and radiative properties of an extreme case of instantaneous loading of the lower troposphere by dust aerosols caused by a "Shamal" dust storm. A low pressure system moved from northern Mediterranean through north Africa into northern Iraq, Baghdad and then reached Kuwait on 26 March 2003 as a dust storm at 07:00 LTC. The severity of the dust storm not only reduced visibility to about 200m but also left a thick suspension of fine dust in the lower troposphere for the following 24 h. Dust concentrations reached $4800\,\mu\mathrm{g\,m^{-3}}$ on 26 March and fluctuated around $1000\,\mu\mathrm{g\,m^{-3}}$ throughout the following day. Ground-based measurements

ACPD
13, 23895–23941, 2013

of AOT on 26 March reached 3.617 and 4.17 on 27 March with the corresponding Ångstrom coefficient $\alpha_{870/440}$ dropping to −0.0234 and −0.0318 respectively reflecting the dominance of coarse-sized particles. MODIS retrieved optical properties exhibited similar extreme values with an average AOD_{550} of 4 and $\alpha_{470/660}$ of approximately 0.5 on 26 March; average AOD_{550} close to 3 and $\alpha_{470/660}$ close to 0.6 on 27 March. Atmospheric model SKIRON was employed to estimate the vertical profile of the dust layer. It was found that the whole dust layer had reached about 6 km above surface level but the bulk of the coarse-sized dust particles were concentrated in the lower 3 km. The source regions of 26 March dust storm were determined using TOMS retrieved aerosol index image. It was found that two source regions supplied the sand and dust that was carried over Kuwait; one was the lower Mesopotamian source region located north of Kuwait and the other was the Rub'al Khali source region located at the southeastern part of the Arabian Peninsula. Dust transport from these two source regions added to the intensity of the fallen dust over Kuwait and expanded the resultant rising dust on 27 March to encompass the middle to eastern parts of the Arabian Peninsula. The instantaneous impact of the dust layer on the radiative flux was calculated at TOA and surface level for both SW and LW components of the electromagnetic spectrum using atmospheric transfer model SBDART. The net RF was dominated by the SW cooling at TOA due to the backscattering of incoming solar radiation and cooling at surface level due to the attenuation of solar radiation by the dust layer. Radiative forcing was calculated for two characteristic surface albedo of desert environment, $R_s = 0.3$ and $R_s = 0.35$. Net RF on 26 March reached $-60\,Wm^{-2}$at TOA and $-175\,Wm^{-2}$ at surface level for $R_s = 0.35$; $-84\,Wm^{-2}$ for TOA and $-195\,Wm^{-2}$ for surface level for $R_s = 0.3$. Radiative forcing on 27 March was slightly higher due to the increase in AOT. Consequently surface temperature dropped on both days by approximately 6°C below its average values. Finally heating/cooling rate in the SW and LW bands were investigated. Heating rate was dominant due to SW absorption by dust aerosols and reached a peak value of $2°\,K\,day^{-1}$ at atmospheric layers located between 3 and 5 km from ground level. On the other hand it was found that the abundance of coarse-sized dust particles enhanced

ACPD
13, 23895–23941, 2013

LW absorption and added a small amount of heating, maximum 0.2° K day^{-1}, at the atmospheric layers adjacent to ground level. This heating decreased rapidly for higher altitude as finer particles replaced coarser ones. At 4 km LW heating switched to cooling and reached a maximum value of −0.1° K day^{-1} at 6 km. Above 7 km both SW and LW heating/cooling rated were reduced to zero. The heating/cooling profile mirrored the SKIRON simulation of dust profile.

Acknowledgements. This work was supported by PAAET fund BE_01_005.

"Analyses and visualizations used in this paper were produced with the Giovanni online data system, developed and maintained by the NASA Goddard Earth Sciences (GES) Data and Information Services Center (DISC)."

Michael Bergun and Giorgi de Siaara for their helpful discussions on radiative forcing.

Nabeel Wilf for providing references.

Mary Winkler for revising the manuscript.

References

Achudume, A. C. and Oladipo, B. O.: Effects of dust storm on health in the Nigerian environment, Biol. Med., 1, 21–27, 2009.

Alizadeh Choobari, O., Zawar-Reza, P., and Sturman, A.: Low level jet intensification by mineral dust aerosols, Ann. Geophys., 31, 625–632, doi:10.5194/angeo-31-625-2013, 2013.

Alpert, P., Kishcha, P., Shtivelman, A., Krichak, S. O., and Joseph, J. H.: Vertical distribution of Saharan dust based on 2.5-year model predictions, Atmos. Res., 70, 109–130, 2004.

Anderson, J., Hardy, E., Roach, J., and Witmer, R.: A land use and land cover classification system for use with remote sensing data. US Geol. Prof. Pap., 964, US Gov. Print. Off., Washington D.C., 1976.

Andreae, T. W., Andreae, M. O., Ichoku, C., Karnieli, A., and Orlovsky L.: Light scattering by dust and anthropogenic aerosol at a remote site in the Negev desert, Israel, J. Geophys. Res., 107, D2, 10.1029/2001JD900252, 2002.

ACPD

13, 23895–23941, 2013

Andrews, E., Sheridan, P. J., Fiebig, M., McComiskey, A., Ogren, J. A., Arnott, P., Covert, D., Elleman, R., Gasparini, R., Collins, D., Jonsson, H., Schmid, B., and Wang, J.: Comparison of methods for deriving aerosol asymmetry parameter, J. Geophys. Res., 111, D05S04, doi:10.1029/2004JD005734, 2006.

Atkinson R.: In the Company of Soldiers, Henry Holt and Company, 337 pp., 2004.

Bierwirth, E., Wendisch, M., Ehrlich, A., Heese, B., Tesche, M., Althausen, D., Schladitz, A., Müller, D., Otto, S., Trautmann, T., Dinter, T., Von Hoyningen-Huene, W., and Kahn, R.: Spectral surface albedo over Morocco and its impact on radiative forcing of Saharan dust, Tellus B, 61, 252–269, doi:10.1111/j.1600-0889.2008.00395.x, 2009.

Berk, A., Bernstein, L. W., and Robertson, D. C.: MODTRAN: A moderate resolution model for LOWTRAN 7, Rep. AFGL-TR-83-0187, 10 pp., 1983.

Carbo, P., Krom, M. D., Homoky, W. B., Benning, L. G., and Herut, B.: Impact of atmospheric deposition on N and P geochemistry in the southeastern Levantine basin, Deep-Sea Res. II., 52, 3041–3053, 2005.

Carlson, T. N. and Benjamin, S.: Radiative heating rates for Sahara dust, J. Atmos. Sci., 37, 193–213, 1980.

Chen, S., Kuo, Y., Ming, W., and Ying, H.: The effect of dust radiative heating on low-level frontogenesis, J. Atmos. Sci., 52, 1414–1420, 1994.

Chylek, P. and Coakley, J. A.: Aerosols and Climate, Science, 183, 75–77, 1974.

Costa, M. J., Sohn, B. J., Levizzani, V., and Silva, A. M.: Radiative Forcing of Asian Dust determined from the Synergized GOME and GMS Satellite Data-A Case Study, J. Meteor. Soc. Jpn., 84, 85–95, 2006.

Griffin, D. W.: Atmospheric Movement of Microorganisms in Clouds of Desert Dust and Implications for Human Health, Clin. Microbiol. Rev., 20, 3, 459-477, 2007.

D'Almeida, G. A.: On the variability of desert aerosol radiative characteristics, J. Geophys. Res., 92, D3, 3017–3026, 1987.

De Villiers, M. P. and Heerden, J. Van: Dust Storms and dust at Abu Dhabi international airport, Weather, 62, 12, 339–343, 2007.

Di Biagio, C., Di Sarra, A., and Meloni D.: Large atmospheric shortwave radiative forcing by Mediterranean aerosols derived from simultaneous ground-based and spaceborne observations and dependence on the aerosol type and single scattering albedo, J. Geophys. Res., 115, D10209, 2010.

ACPD
13, 23895–23941, 2013

Di Sarra, A., Pace, G., D. Meloni, L. De Silvestri, S. Piacentino, and Monteleone F.: Surface shortwave radiative forcing of different aerosol types in the central Mediterranean, Geophys. Res. Lett., 35, L02714, doi:10.1029/2007GL032395, 2008.

Gao, T., Su, L., Ma, Q., Li, H., Li, X., and Yu, X.: Climatic analyses on increasing dust storm frequency in the springs of 2000 and 2001 in inner Mongolia, Int. J. Climatol., 23, 1743–1755, 2003.

Gillette, D. A.: Fine particle emissions due to wind erosion, Trans. Am. Soc. Agric. Eng., 20, 891–897, 1977.

Gobeli, D., Schloesser, H., and Pottberg, T.: Met One Instruments BAM-1020 Beta Attenuation Mass Monitor US-EPA $PM_{2.5}$ Federal Equivalent Method Field Test Results, A-485-AWMA, 11 pp., 2008.

Goudie, A. S.: Dust Storms: Recent developments, J. Environ. Manage., 90, 89–94, 2009.

Goudi A. S. and Middleton N. J.: The changing frequency of dust storms through time, Clim. Chang., 20, 197–225, 1992.

Griffin, D. W.: Atmospheric movement of microorganisms in clouds of desert dust and implications for human health, Clin. Microbiol. Rev., 20, 459–477, 2007.

Griffin, D. W. and Kellogg, C. A.: Dust Storms and Their Impact on Ocean and Human Health: Dust in Earth's Atmosphere, Eco. Health, 1, 284–295, 2004.

Haywood, J. and Boucher, O.: Estimates of Radiative Forcing, Rev. Geophys., 38, 513–543, 2000.

Herut, B., Zohary, T., Krom, M. D., Mantoura, F. R., Pitta, P., Psarra, S., Rassoulzadegan, F., Tanaka, T., and Thingstad, T. F.: Response of East Mediterranean surface water to Saharan dust: On-board microcosm experiment and field observation, Deep- Sea Res. II, 52, 3024–3040, 2005.

Haywood, J. M., Johnson, B. T., Osborne, S. R., Baran, A. J., Brooks, M., Milton, S. F, Mulcahy, J., Walters, D., Allan, R. P., Klaver, A., Formenti, P., Brindley, H. E., Christopher, S., and Gupta, P.: Motivation, rationale and key results from the GERBILS Saharan dust measurement campaign, Q. J. Roy. Meteorol. Soc., 137, 1106–1116, doi:10.1002/qj.797, 2011.

Husar, R. B., Tratt, D. M., Schichtel, B. A., Falke, S. R., Li, F., Jaffe, D., Gass, S., Gill, T., Laulainen, N. S., Lu, F., Reheis, M. C., Chun, Y., Westphal, D., Holben, B. N., Gueymard, C., McKendry, I., Kuring, N., Feldman, G. C., McClain, C., Frouin, R. J., Merrill, J., DuBois, D., Vignola, F., Murayama, T., Nickovic, S., Wilson, W. E., Sassen, K., Sugimoto, N., and Malm, W. C.: Asian dust events of April 1998, J. Geophys. Res., 106, 18317–18330, 2001.

ACPD
13, 23895–23941, 2013

Intergovernmental Panel on Climate Change (IPCC): Changes in atmospheric constituents and radiative 5 forcing: Climate change: the physical science basis, Cambridge University Press, New York, USA, and Cambridge, UK, 2007.
Janjic, Z. I.: Nonlinear advection schemes and energy cascade on semi-staggered grids, Mon. Weather Rev., 112, 1234–1245, 1984.
Jickells, T. D., Z. S. An, K. K. Andersen, A. R. Baker, G. Bergametti, N. Brooks, J. J. Cao, P. W. Boyd, R. A. Duce, K. A. Hunter, H. Kawahata, N. Kubilay, J. laRoche, P. S. Liss, N. Mahowald, J. M. Prospero, A. J. Ridgwell, I. Tegen and Torres R.: Global iron connections between desert dust, ocean biogeochemistry, and climate, Science, 308, 5718, 67–71, 2005.
Kallos, G., Nickovic, S., Jovic, D., Kakaliagou, O., Papadopoulos, A., Misirlis, N.,Boukas, L., and Mimikou, N.: The ETA model operational forecasting system and its parallel implementation, 30 Proceedings of the 1st Workshop on Large- Scale Scientific Computations, 7–11 June 1997, Varna, Bulgaria, 15 pp., 1997b.
Kallos, G., Papadopoulos, A., Katsafados, P., and Nickovic, S.: Transatlantic Saharandust transport: Model simulation and results, J. Geophys. Res., 111, D09204, doi:10.1029/2005JD006207, 2006.
Kaskaoutis D. G., Kambezidis, H. D., Nastos, P. T. and Kosmopoulos, P. G.: Study onan intense dust storm over Greece, Atmos. Envriron., 42, 6884-6896, 2008.
Key, J.: Streamer User's Guide, Cooperative Institute for Meteorological Satellite Studies, University of Wisconsin, 96 pp., 2001.
Kneizys, F. X., Shettle, E. P., Gallery, W. O., Chetwynd, J. H. Abreu, L. W., Selby, J. E. A., Clough, S. A., and Fenn, R. W.: Atmospheric transmittance/radiance: Computer code LOWTRAN 6, Rep. AFGL-TR-83-0187, 200 pp., 1983.
Kutiel, H. and Fruman, F.: Dust storms in the middle east: sources of origin and their temporal characteristics, Indoor. Buil. Environ., 12, 419–426, 2003.
Lemaître, C., Flamant, C., Cuesta, J., Raut, J.-C., Chazette, P., Formenti, P., and Pelon, J.: Radiative heating rates profiles associated with a springtime case of Bodélé and Sudan dust transport over West Africa, Atmos. Chem. Phys., 10, 8131–8150, doi:10.5194/acp-10-8131-2010, 2010.
Leski T. A., Malanoski, A. P., Gregory, M. J., Lin, B., and Stenger, D. A.: Application of a Broad-Range Resequencing Array for Detection of Pathogens in Desert Dust Samples from Kuwait and Iraq, Appl. Environ. Microbiol., 77, 4285–4292, 2011.

ACPD
13, 23895–23941, 2013

Lio, H. and Seinfeld, J. H.: Radiative forcing by mineral dust aerosols: sensitivity to key variables, J. Geophys. Res., 103, 31637–31645, 1998.
Lyles, L.: Basic wind erosion processes, Agric. Ecosyst. Environ., 22/23, 91–101, 1988.
Mahowald, N. M., Baker, A. R., Bergametti, G., Brooks, N., Duce, R. A., Jickells, T. D., Kubilay, N., Prospero, J. M., and Tegen, I.: Atmospheric global dust cycle and iron inputs to the ocean, Global Biogeochem. Cy., 19, GB4025, doi:10.1029/2004GB002402, 2005.
Mallet, M., Tulet, P., Serça, D., Solmon, F., Dubovik, O., Pelon, J., Pont, V., and Thouron, O.: Impact of dust aerosols on the radiative budget, surface heat fluxes, heating rate profiles and convective activity over West Africa during March 2006, Atmos. Chem. Phys., 9, 7143–7160, doi:10.5194/acp-9-7143-2009, 2009.
Markowicz, K. M., Flatau, P. J., Remiszewska, J., Witek, M., Reid, E. A., Reid, J. S., Bucholtz, A., and Holben, B.: Observations and Modeling of the Surface Aerosol Radiative Forcing during UAE^2, J. Atmos. Sci., 65, 2877–2891, 2008.
Marshall, S.F., Covert, D. S. and Charlson, R. J.: Relationship between asymmetry parameter and hemispheric backscatter ratio: implications for climate forcing by aerosols, Appl. Optics, 34, 27, 6306-6311, 1995.
McConnell, C. L., Highwood, E. J., Coe, H., Formenti, P., Anderson, B., Osborne, S., Nava, S., Desboeufs, K., Chen, G., and Harrison, M. A. J.: Seasonal variations of the physical and optical characteristics of Saharan dust: Results from the Dust Outflow and Deposition to the Ocean (DODO) experiment, J. Geophys. Res., 113, D14S05, doi:10.1029/2007jd009606, 2008.
Mesinger, F.: A blocking technique for representation of mountains in atmospheric models, Riv. Meteorol. Aeronaut., 44, 195–202, 1984.
Middleton, N. J.,: Dust storms in the Middle East, J. Arid. Environ., 10, 83–96, 1986a.
Miller, D. A., and White, R. A.: A conterminous United States multilayer soil characteristics data set for regional climate and hydrology modeling, Earth Interact., 2, 1–26, 1998.
Mohalfi, S., Bedi, H. S., Krishnamurti, T. N., and Cocke, S. D.: Impact of short wave radiative effects of dust aerosols on the summer season heat low over Saudi Arabia, Mon. Weather Rev., 126, 3153–3168, 1998.
Ogunjobi, K. O., Kim, Y. J., and He, Z.: Aerosol optical properties during Asian dust storm episodes in South Korea, Theor. Appli. Climatol., 76, 65–75, 2003.
Park, S., Ahn, H., and Park, M.: Direct shortwave radiative forcing of the Asian dust aerosol on dust emission, Theor. Appl. Climatol., 101, 1–2, 179–190, 2010.

ACPD
13, 23895–23941, 2013

Osborne, S. R., Johnson, B. T., Haywood, J. M., Baran, A. J., Harrison, M. A. J., and McConnell, C. L.: Physical and optical properties of mineral dust aerosol during the Dust and Biomass-burning Experiment, J. Geophys. Res., 113, D00C03, doi:10.1029/2007jd009551, 2008.
Pandithurai, G., Dipu, S., Dani, K. K., Tiwari, S., Bisht, D. S., Devara, P. C. S., and Pinker R. T.: Aerosol radiative forcing during dust events over New Delhi, India, J. Geophys. Res., 113, D13209, doi:10.1029/2008JD009804, 2008.
Pérez, C., Nickovic, S., Baldasano, J. M., Sicard, M., Rocadenbosch, F., and Achorro, V. E.: A long Saharan dust event over the western Mediterranean: Lidar, Sunphotometer observations, and regional dust modeling, J. Geophys. Res., 111, D15214, doi:10.1029/2005JD006579, 2006.
Perrone, T. J.: Winter Shamal in the Persian Gulf, Technical Report, Naval Environmental Prediction Research Facility, Monterey, California 93940, 1979.
Petty, G. M.: A First Course In Atmospheric Radiation, Sundog Publishing, 458 pp., 2006.
Prasad, A. K. and Singh, R. P.: Changes in aerosol parameters during major dust storm events (2001–2005) over Indo-Gangetic plains using AERONET and MODIS data, J. Geophys. Res., 112, D09208, doi:10.1029/2006JD007778, 2007.
Prospero, J. M., Ginoux, P., Torres, O., Nicholson, S. E., and Gill, T. E.: Environmental characterization of global sources of atmospheric soil dust identified with the Nimbus-7 Total Ozone Mapping Spectrometer (TOMS) absorbing aerosol product, Rev. Geophys., 40, 2-1–2-31, doi:10.1029/2000RG000095, 2002.
Quijano A. L., Sokolik, I. N., and Toon, O. B.: Radiative heating rates and direct radiative forcing by mineral dust in cloudy atmospheric conditions, J. Geophys. Res., 105, 12207–12219, 2000.
Ravi, S., Breshears, D. D., Huxman, T. E., and D'Odorico, P.: Land degradation in drylands: Interactions among hydrologic–aeolian erosion and vegetation dynamics, Geomorphology, 116, 3–4, 236–245, 2010.
Ricchiazzi, P., Yang, S., Gautier, C., and Sowle, D.: SBDART: A research and teaching software tool for plane-parallel radiative transfer in the Earth's atmosphere, Bull. Am. Meteorol. Soc., 79, 2101–2114, 1998.
Sabbah, I., Ichoku, C., Kaufman, Y. J., and Remer, L.: Full year cycle of desert dust spectral optical thickness and precipitable water vapor over Alexandria Egypt, J. Geophys. Res., 106, 18305–18316, 2001.

ACPD
13, 23895–23941, 2013

Saeed. T. and Al-Dashti, H.: Optical and physical characterization of “Iraqi freedom” dust storm, a case study, Theor. Appl. Climatol., 104, 123–137, 2010.
Seinfeld, J. H. and Pandis, S. N.: Atmospheric Chemistry and Physics: From Air Pollution to Climate Change, 1326 pp., John Wiley, New York, 1998.
Sharma, D., Singh, D., and Kaskaoutis, D. G.: Impact of Two Intense Dust Storms on Aerosol Characteristics and Radiative Forcing over Patiala, Northwestern India, Adv. Meteorol., 2012, 13 pp., doi:10.1155/2012/956814, 2012.
Stephens, G. L.: Remote sensing of the lower atmosphere, Oxford University Press, 523 pp., 1994.
Simonson, R. W.: Airborne dust and its significance to soils, Geoderma., 65, 1–43, 1995.
Sokolik, I. N. and Golitsyn, G. S.: Investigation of optical and radiative properties of dust aerosols, Atmos. Environ., 27A, 2509-2517, 1993.
Sokolik, I. N. and Toon, O. B.: Incorporation of mineralogical composition into models of the radiative properties of mineral aerosol from UV to IR wavelengths, J. Geophys. Res., 104, 9423–9444, 1999.
Sokolik, I. N., Andronova, A. V., and Johnson, T. C.: Complex refractive index of atmospheric dust aerosol, Atmos. Environ., 27A, 2495–2502, 1993.
Spyrou, C., C. Mitsakou, G. Kallos, P. Louka, and Vlastou, G.: An improved limited area model for describing the dust cycle in the atmosphere, J. Geophys. Res., 115, D17211, doi:10.1029/2009JD013682, 2010.
Stamnes, K., Tsay, S. C., Wiscombe, W., and Jayaweera, K.: Numerically stable algorithm for discrete-ordinate-method radiative transfer in multiple scattering and emitting layered media, Appl. Opt., 27, 2502–2509, 1988.
Stefanski, R. and Sivakumar, M. V. K.: Impacts of sand and dust storms on agriculture and potential agricultural applications of a SDSWS, IOP Conf. Ser. Earth Environ. Sci., 7, 012016, 2009.
Swap, R., Garstang, M., Greco, S., Talbot, R., and Kallberg, P.: Sahara dust in the Amazon basin, Tellus B, 44, 133–149, 1992.
Tanré, D., Haywood, J., Pelon, J., Léon, J. F., Chatenet, B., Formenti, P., Francis, P., Goloub, P., Highwood, E. J., and Myhre, G.: Measurement and modeling of the Saharan dust radiative impact: Overview of the Saharan Dust Experiment (SHADE), J. Geophys. Res., 108, 8574, doi:10.1029/2002jd003273, 2003.

ACPD
13, 23895–23941, 2013

Tegen, I. and Lacis, A. A.: Modeling of particle influence on the radiative properties of mineral dust aerosol, J. Geophys. Res., 101, 19237–19244, 1996.
Tsolmon, R., Ochirkhuyag, L., and Sternberg, T.: Monitoring the source of trans-national dust storms in north east Asia, Int. J. Digit. Earth, 1, 119–129, 2008.
Washington, R., Todd, M., Middleton, N. J., and Goudie, A. S.: Dust-Storm source areas determined by the Total Ozone Monitoring Spectrometer and surface observations, Ann. Amer. Geogr., 93, 297–313, 2003.
Wilkerson, W. D.: Dust and sand forecasting in Iraq and adjoining countries, Technical Report, Air Weather Services, Scott AFB, IL 62225-5008, 1991.
Wilson, R. and Spengler, J.: Particles in Our Air: Concentrations and Health Effects, Harvard Univ. Press., 254 pp., 1996.
Xia, X. and Zong, X.: Shortwave versus longwave direct radiative forcing by Taklimakan dust aerosols, J. Geophys. Res., 36, L07803, doi:10.1029/2009GL037237, 2009.
Xu, J., Bergin, M. H., Greenwald, R., and Russell, P. B.: Direct aerosol radiative forcing in the Yangtze delta region of China: Observation and model estimation, J. Geophys. Res., 108, 4060–4072, 2003.
Xuana, J., Sokolik I. N., Hao, J., Guo, F., Mao, H., and Yang, G.: Identification and characterization of sources of atmospheric mineral dust in East Asia. Atmos. Environ., 38, 6239–6252, 2004.
Youlin, Y., Squires, V. R., and Qu, L.: Global alarm: Dust and sandstorms from the world's drylands, UN Bejing, 325 pp., 2002.
Zender, C. S., Bian, H., and Newman, D.: Mineral Dust Entrainment and Deposition (DEAD) model: Description and 1990s dust climatology, J. Geophys. Res., 108, 4416, doi:10.1029/2002JD002775, 2003.

ACPD
13, 23895–23941, 2013

Table 1. The dust storm optical and physical properties together with the average PM_{10} and the corresponding meteorological parameters at 11:30 LT (+3 UTC).

	26 March	27 March
τ_{675}	3.617	4.17
$\alpha_{870/440}$	−0.0234	−0.0318
PM_{10} ($\mu g\,m^{-3}$)	1770	2641
WS ($m\,s^{-1}$)	10.5	4.5
HV (km)	0.4	1.25
WD	NW	SW, W
WP	DS	S

ACPD
13, 23895–23941, 2013

Table 2. Vertical distribution of the dust layer.

	26 March		27 March	
	Terra	Aqua	Terra	Aqua
AOD_{550}	3.3 ± 2	5	3.1 ± 2.36	2.8 ± 2
$\alpha_{470/660}$	0.48 ± 0.02	–	0.6	0.58
MC ($\mu g\, m^{-2}$)	–	117.8 ± 33.9	–	24.7
AI (TOMS)	2.95 ± 0.66		3.77 ± 0.93	

ACPD
13, 23895–23941, 2013

Table 3. The critical input parameters of SBDART model.

	26 March	27 March
λ (μm)	0.675	0.675
τ_λ	3.617	4.17
ω	0.984	0.984
g	0.73	0.73
HV (km)	0.4	1.25
RH	0.25	0.39
CSZA	0.88	0.88

ACPD
13, 23895–23941, 2013

Table 4. Instantaneous shortwave and longwave DRF estimation for 26–27 March 2003 at two surface reflectance at 11:30 LT (+3 UTC).

		26 March		27 March	
		$R_s = 0.3$	$R_s = 0.35$	$R_s = 0.3$	$R_s = 0.35$
SW (Wm^{-2})	DRF_{TOA}	−95	−70	−119	−93
	DRF_{surf}	−204	−183	−218	−195
LW (Wm^{-2})	DRF_{TOA}	11	10	12	11
	DRF_{surf}	9	8	10	9
Total DRF (Wm^{-2})	$DRF_{\circ,TOA}$	−84	−60	−107	−82
	$DRF_{\circ,surf}$	−195	−175	−208	−186
	$DRF_{\circ,atm}$	111	115	107	104

ACPD
13, 23895–23941, 2013

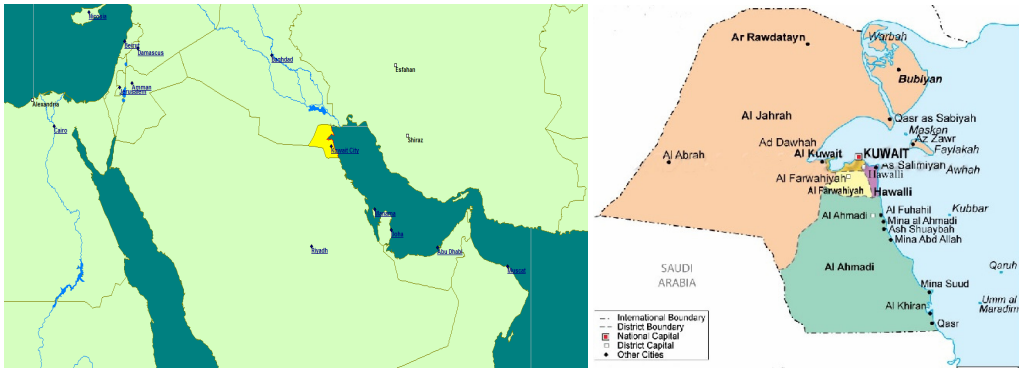

Fig. 1. Kuwait geographical location within the Arabian Peninsula (yellow area, left), and an enlarged map of Kuwait (right).

ACPD
13, 23895–23941, 2013

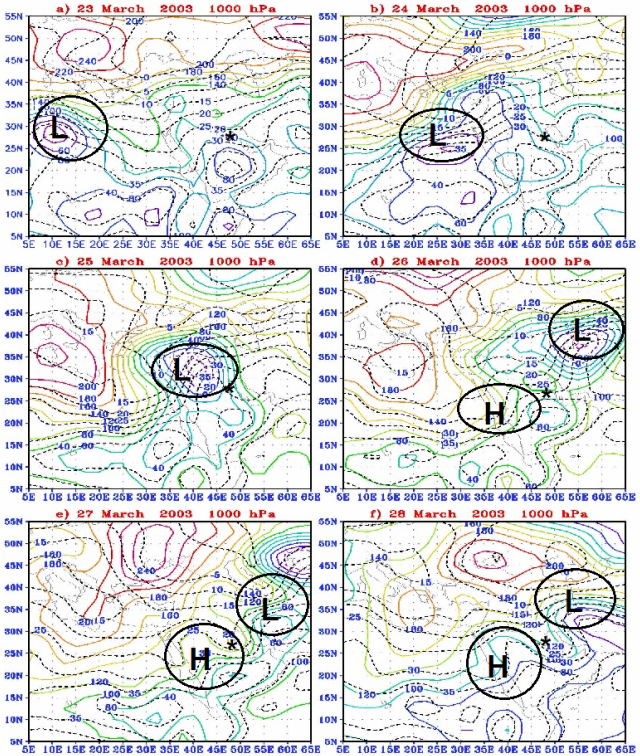

Fig. 2. Contour lines (solid lines) and isotherms (dotted lines) at 1000 mb for the period of 23–28 March. The ellipses and circles show the low (L) and high (H) pressure zones. The star symbol "*" indicates the location of Kuwait.

ACPD
13, 23895–23941, 2013

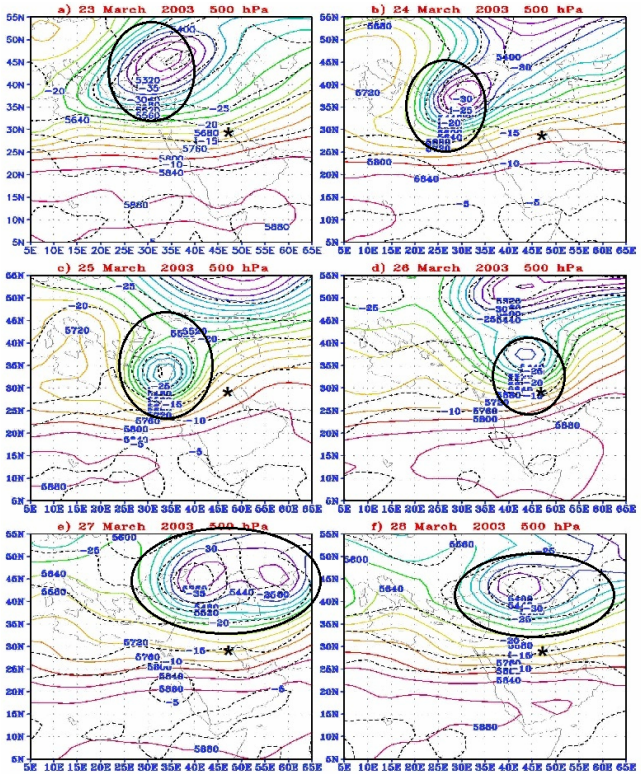

Fig. 3. Contour lines (solid lines) and isotherms (dotted lines) at 500 mb for the period of 23–28 March 2003. The star symbol "*" indicates the location of Kuwait.

ACPD
13, 23895–23941, 2013

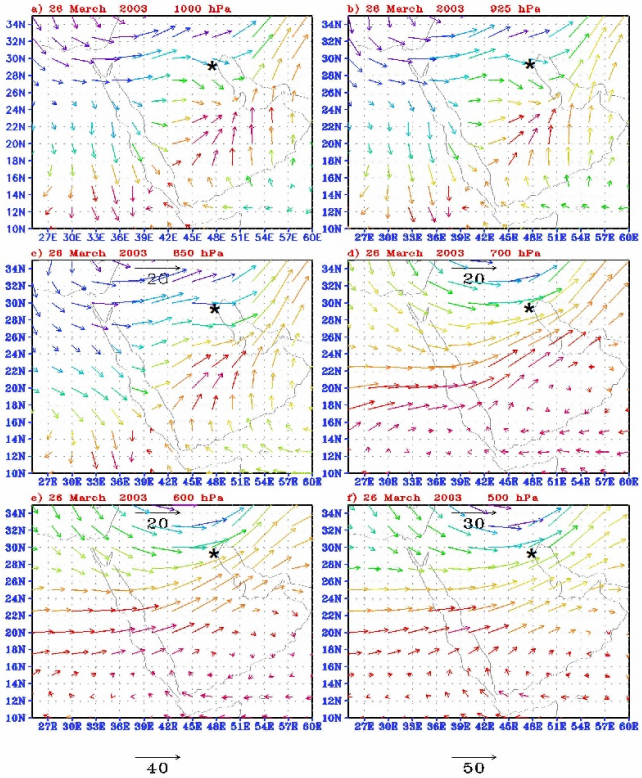

Fig. 4. Wind fields at different geopotential levels on 26 March 2003. The star symbol "*" indicates the location of Kuwait.

ACPD
13, 23895–23941, 2013

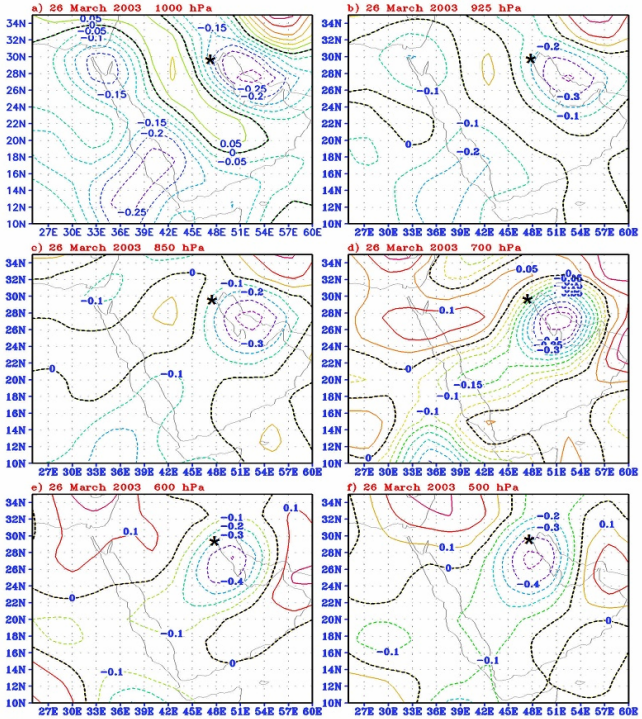

Fig. 5. Horizontal distribution of the vertical motion (ω) at different geopotential heights on 26 March. The star symbol "*" indicates the location of Kuwait.

ACPD
13, 23895–23941, 2013

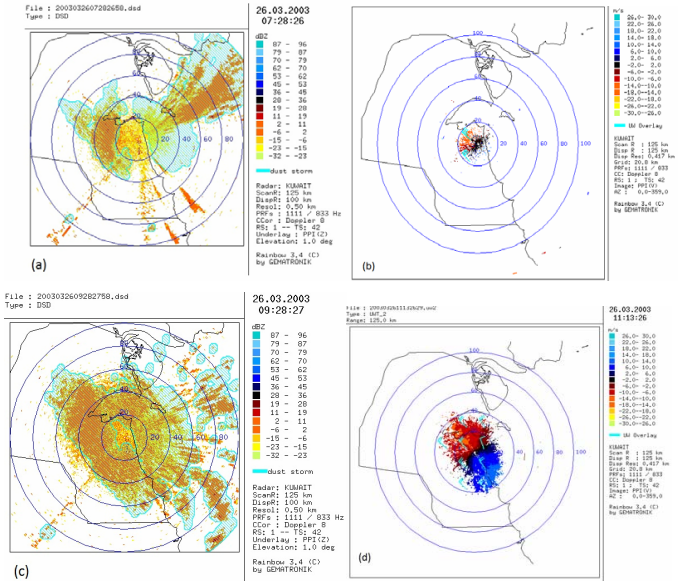

Fig. 6. The radar display of reflectivity Z and radial velocity ($m\,s^{-1}$) at the beginning of the dust storm, approximately 07:30 LT, **(a)** and **(b)** and at a later stage, approximately 09:30 LT, **(c)** and **(d)**.

ACPD
13, 23895–23941, 2013

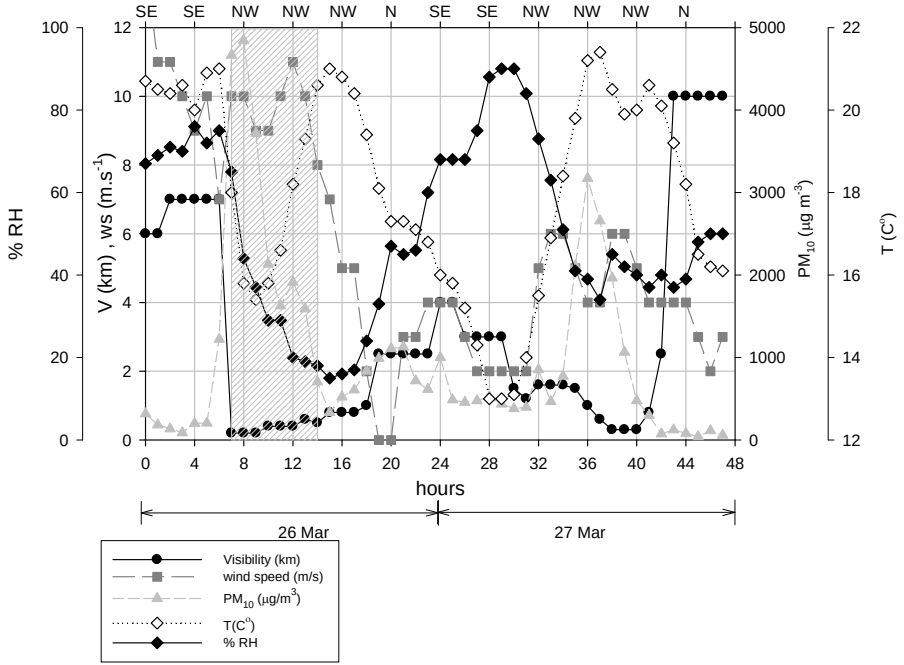

Fig. 7. Hourly variation of visibility, V (km), wind speed, WS ($m\,s^{-1}$), (PM_{10}), temperature *T* (°C) and wind direction (top axis) for 26–27 March2003. The shaded area represents dust storm hours at Kuwait local time (+3 UTC).

ACPD
13, 23895–23941, 2013

Aerosols characteristics and direct radiative forcing

T. M. Saeed

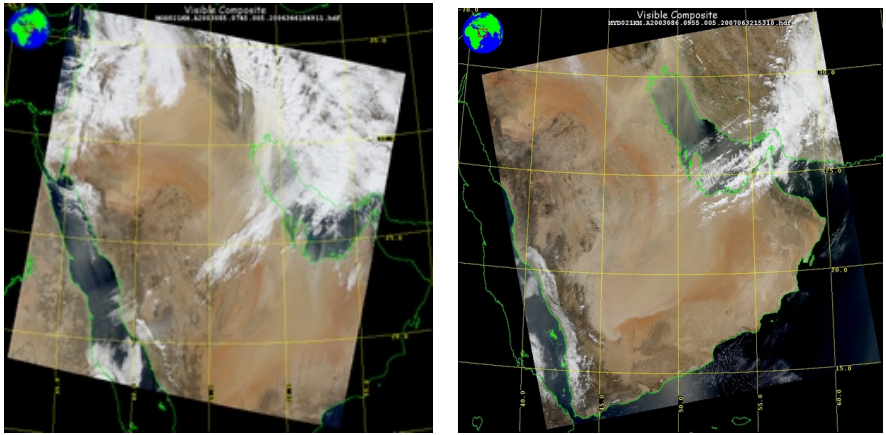

Fig. 8. Terra-MODIS RGB image captured on 26 March shows the dust front moving from the northwesterly direction into Kuwait, (left). The 27 March rising dust capture by Aqua-MODIS shows clearly a thin layer of dust covering most of the Arabian (Persian) Gulf, (right).

ACPD
13, 23895–23941, 2013

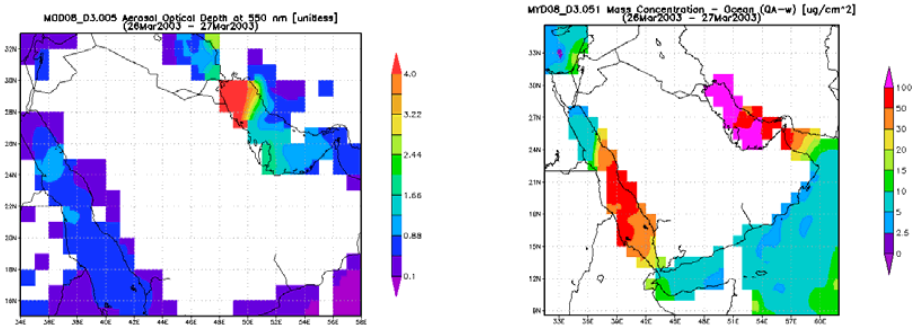

Fig. 9. Terra-MODIS retrieved image of (left) and Aqua-MODIS retrieved image of mass concentration ($\mu g\,m^{-2}$) (right). The highest mass concentration is exhibited over the Arabian (Persian) Gulf.

ACPD
13, 23895–23941, 2013

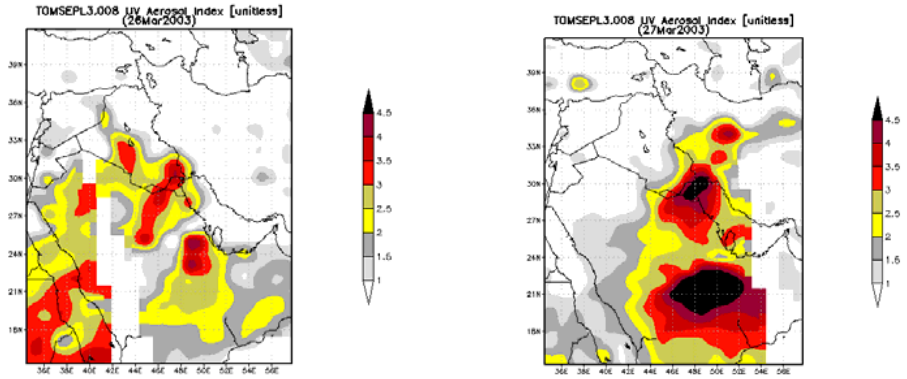

Fig. 10. Aerosol index distribution across the Arabian Peninsula for 26 March dust storm (left) and 27 March (right).

ACPD
13, 23895–23941, 2013

Fig. 11. Rub'al Khali (colored red) is one of the most prolific dust-producing regions across the globe. It dominates the southern parts of the Arabian Peninsula.

ACPD
13, 23895–23941, 2013

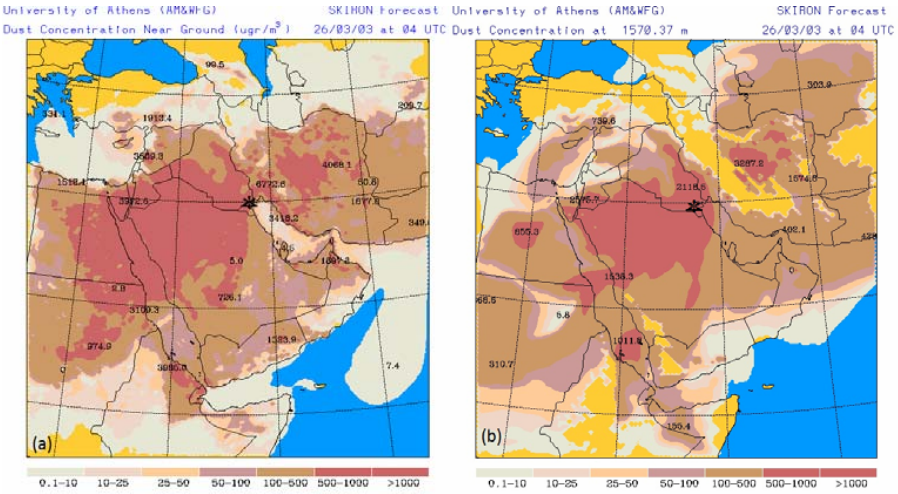

Fig. 12. Dust concentration ($\mu g\,m^{-3}$) on 26 March for **(a)** near ground level and **(b)** at an elevation of 1570 m from ground level. The "*" indicates Kuwait location.

ACPD
13, 23895–23941, 2013

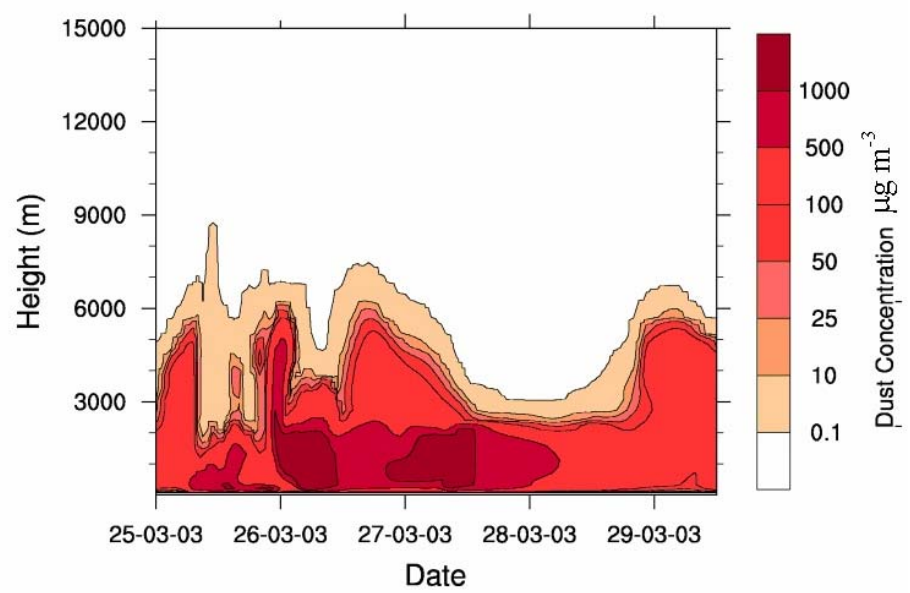

Fig. 13. The SKIRON atmospheric modeling of dust vertical profile for the period of 25–29 March 2003. Two pockets of high dust concentration are generated around 26–27 March.

ACPD
13, 23895–23941, 2013

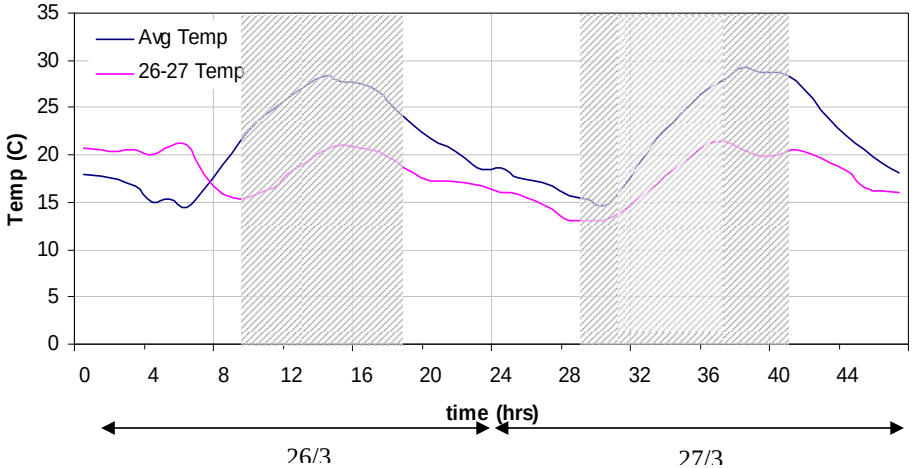

Fig. 14. Hourly variation of surface temperature on 26–27 March in comparison to hourly average temperature variations under dust free conditions based on temperature records of previous years. The shaded area represents dust storm hours.

ACPD
13, 23895–23941, 2013

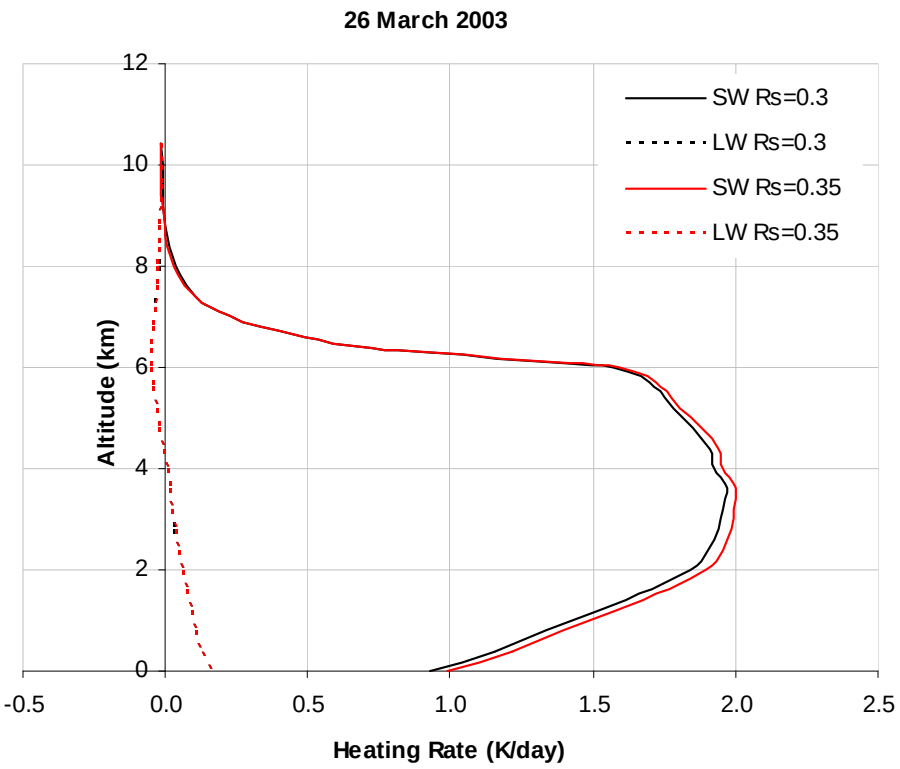

Fig. 15. SW and LW heating/cooling rates variation with altitude on 26 March for surface reflectivity of 0.3 and 0.35. Most of the heating is well within the dust layer and drops sharply to zero above 6 km which is the upper boundary of the dust layer.

ACPD
13, 23895–23941, 2013